Construction and Building Materials 345 (2022) 128281

Contents lists available at ScienceDirect

Construction and Building Materials

journal homepage: www.elsevier.com/locate/conbuildmat

# Experiments and modelling to understand $FeCO_3$ cement formation mechanism: time-evolution of $CO_2$-species, dissolved-Fe, and pH during $CO_2$-induced dissolution of Fe(0)

Sumit Srivastava [a,b,d,*], Rob Jacklin [c], Ruben Snellings [a], Richard Barker [c], Jeroen Spooren [a], Pegie Cool [b]

[a] Sustainable Materials Management, Flemish Institute of Technological Research (VITO), Boeretang 200, B-2400 Mol, Belgium
[b] Laboratory of Adsorption and Catalysis, Dept. of Chemistry, University of Antwerp, B-2610 Wilrijk, Belgium
[c] Institute of Functional Surfaces, School of Mechanical Engineering, University of Leeds, Leeds LS2 9JT, UK
[d] Fibre and Particle Engineering Research Unit, University of Oulu, Oulu 90014, Finland

ARTICLE INFO

*Keywords:*
Accelerated carbonation
Siderite ($FeCO_3$)-cement
$CO_2$-corrosion
Fe-dissolution
Carbonate cement
$CO_2$-utilization

ABSTRACT

$FeCO_3$ cement can be produced by reacting $CO_{2(aq)}$ and particulate-Fe(0). *Process conditions* and *solution compositions* influence cement properties through kinetics of Fe-dissolution and $FeCO_3$-precipitation. This study investigates Fe-dissolution in dilute systems (water(wt.)/Fe(wt.) = 1000) at 30/60 °C, and 1/10 barg $CO_2$-pressures. Experimentally, time-evolution of *solution composition* shows increased [Fe] and solution-pH. As a proxy for high-pressure in-situ experiments, a modeling approach is developed to quantify with [Fe]-increase, the: decreased $[H^+]$, increased $[HCO_3^-]/[OH^-]/[CO_3^{2-}]$, and undisturbed $[CO_{2(aq)}]/[H_2CO_3]$. Fe-dissolution rates increase with: (a) pH-decrease with increased $CO_2$-pressure, and (b) faster kinetics at higher temperatures, even with higher pH. Experimental and modeled pH are comparable at 1 bar, two causes are discussed for it being ~ 1.2 times at 10 barg: $CO_2$-depressurization, and Fe-precipitation. Lower $CO_2$-mediated dissolution activation energies of ~ 30 (1 barg) and ~ 20 kJ/mol (10 barg) compared to strong acids (~60 kJ/mol) are attributed to buffering action of $CO_{2(aq)}$.

## 1. Introduction

Over the past decade, several studies have explored the possibility to produce $FeCO_3$-cement by accelerated carbonation of particulate Fe(0) [1-9]. In addition to academic research, the technology has also received significant interest for its industrial application, including marketable product development (for instance Ferrock™) [10-13]. While these studies have focused on the engineering properties of the $FeCO_3$-cement, the mechanism by which $CO_2$ reacts with Fe(0) for the formation of $FeCO_3$-cement in these systems is still not well understood. The objective of the present study is to gain a deeper understanding of the underlying reactions.

$FeCO_3$ cement formation by accelerated carbonation of Fe(0) in the relevant Fe-$CO_2$-$H_2O$ systems involves at least two main steps [5,14]: (a) Fe-dissolution, and (b) precipitation of dissolved-Fe as products such as Fe-carbonates, Fe-(hydro)oxides. Among these, Fe-dissolution is assisted by the lowering of the solution pH by acidic species $(H^+_{(aq)}/H_2CO_3/HCO_3^-)$ resulting from $CO_2$ dissolution in water according to Reaction 1-Reaction 5 [15,16]. Consequently, Fe-dissolution proceeds through coupled anodic Reaction 6 [14,17] and individual cathodic reactions (Reaction 7-Reaction 10) [18-20]. The dissolved $Fe^{2+}$ precipitates as $FeCO_3$ mainly through Reaction 11 with $CO_3^{2-}(aq)$, but also through a two-step reaction with $HCO_3^-(aq)$ (Reaction 12) [21]. As the concentration of dissolved-Fe in the solution increases, the pH of the solution is also expected to increase, and the concentrations of species resulting from Reaction 1-Reaction 5 $(H^+/H_2CO_3/HCO_3^-/CO_3^{2-}/OH^-)$ are consequently expected to shift towards the new equilibrium. Therefore, the concentration of the different ionic species in the solutions are expected to evolve continuously as the [Fe] in the solution increases. Since the concentrations of these species have significant influences on the underlying reactions, their time-evolution with increasing Fe-dissolution needs to be understood. This study uses the experimentally observed pH and $[Fe^{2+}]$ to model the evolution of these

* Corresponding author.
*E-mail address:* sumit.srivastava@oulu.fi (S. Srivastava).

https://doi.org/10.1016/j.conbuildmat.2022.128281
Received 2 January 2022; Received in revised form 10 June 2022; Accepted 27 June 2022
Available online 3 July 2022

species. For this, the established modeling techniques for $CO_2$ water chemistries and $CO_2$-induced Fe-dissolution are adapted to suitably define the systems in which pH is allowed to evolve with [Fe]. Comparisons of experimental and modeling results are utilized to elucidate the reaction mechanisms by which $CO_2$-induced Fe-dissolution occurs.

**$CO_2$-dissolution in water**

Reaction 1: $CO_{2\,(g)} \rightleftharpoons CO_{2\,(aq)}$

Reaction 2: $CO_{2\,(aq)} + H_2O_{(l)} \rightleftharpoons H_2CO_{3\,(aq)}$

Reaction 3: $H_2CO_{3\,(aq)} + H_2O_{(l)} \rightleftharpoons HCO_3^-(aq) + H^+_{(aq)}$

Reaction 4: $HCO_3^-(aq) + H_2O_{(l)} \rightleftharpoons CO_3^{2-}(aq) + H^+_{(aq)}$

Reaction 5: $H_2O_{(l)} \rightleftharpoons H^+_{(aq)} + OH^-_{(aq)}$

**Anodic dissolution of Fe**

Reaction 6: $Fe^0 \rightarrow Fe^{2+}_{(aq)} + 2e^-$.

**Cathodic reactions during Fe-dissolution**

Reaction 7: $2H^+_{(aq)} + 2e^- \rightarrow H_{2(g)}$

Reaction 8: $2H_2O_{(l)} + 2e^- \rightarrow H_{2(g)} + 2OH^-_{(aq)}$

Reaction 9: $2H_2CO_{3\,(aq)} + 2e^- \leftrightarrow 2HCO_3^-(aq) + H_{2(g)}$

Reaction 10: $2HCO_3^-(aq) + 2e^- \leftrightarrow 2CO_3^{2-}(aq) + H_{2(aq)}$

**$FeCO_3$-precipitation reactions**

Reaction 11: $Fe^{2+}_{(aq)} + CO_3^{2-}(aq) \rightarrow FeCO_{3(aq)}$

Reaction 12: $Fe^{2+}_{(aq)} + 2HCO_3^-(aq) \rightarrow Fe(HCO_3)_{2(s)} \rightarrow FeCO_{3(s)} + CO_{2(g)} + H_2O_{(l)}$

In the $H_2O$-Fe systems with a given type and amount of powdered Fe (0) mixed at a constant $H_2O$/Fe ratio, the process conditions such as temperature and $CO_2$-pressure can significantly influence the kinetics of the underlying reactions [5,6,10]. These dependencies are usually exploited to improve the mechanical properties of the respective $FeCO_3$ cement by improving the phase composition and microstructure of the carbonation products. However, simultaneous occurrences of Fe-dissolution and the $FeCO_3$-precipitation convolutes the understanding of the influences of temperature/$CO_2$-pressure individually on these underlying reactions. In this context, this study is focused especially on the understanding of the $CO_2$-induced Fe-dissolution. For this, stirred dilute solutions with a high $H_2O$/Fe ratio of 1000 (w/w) are used for the experiments to minimize the precipitation of dissolved-Fe. To understand the influence of temperature and $CO_2$-pressures, two temperatures (30 and 60 ℃) and two $CO_2$-pressures (1 and 10 barg) are studied.

The overall reaction of $CO_2$ with Fe in an aqueous solution can also be significantly influenced by the presence of additives during carbonation, such as Si-rich sources (for instance ashes and slags), Ca-rich sources (such as calcite), organic acids [1,4,6,10,22]. These additives influence the underlying reactions of Fe with $CO_2$ through several mechanisms: for instance, through changes in solution chemistry and pH, through chemical complexation [1,21]. With the time-evolution of the solution led by an increase in [Fe] and pH, possibilities of similar mechanisms are explored in this study [23]. For a better understanding of the role of acidic species from $CO_2$-$H_2O$ systems in Fe-dissolution, the dissolution rates and the activation energies are also calculated.

Therefore, the underlying steps in $FeCO_3$ formation need further understanding. These steps include: (a) the dissolution of $CO_2$ in water to form $H^+/H_2CO_3/HCO_3^-/CO_3^{2-}/OH^-$ and the consequent decrease in the solution pH to 3.5–4.5, (b) the dissolution reaction of Fe(0) to release $Fe^{2+}$ in the solution, which is promoted by the $H^+/H_2CO_3/HCO_3^-$, (c) the subsequent increase in the solution pH (due to $Fe^{2+}$ release), (d) the precipitation of $FeCO_3$, mainly by the reaction of $Fe^{2+}$ with $HCO_3^-$, $and CO_3^{2-}$. The objectives of this work are to: (a) experimentally follow the increase in the [Fe] and pH of the solutions at four combinations of temperature and $CO_2$-pressure, (b) use this data to model the consequent changes in the concentrations of all the other solution species, (c) compare the experimental and modelled pH. Moreover, the $CO_2$-mediated activation energy for Fe-dissolution is also calculated.

## 2. Materials and methods

### 2.1. Materials

Particulate Fe(0) (*Alfa Aesar*, −200 mesh, 99+%, metal basis), deionized MilliQ water, and pure $CO_{2(g)}$ were the only three reactants used. Efforts were made to remove the ultrafine Fe(0) particles from the samples. For this, 30 g of the powdered sample was diluted in ethanol, and the solution was ultrasonicated for 5 min. Subsequently, after allowing about two minutes of settling time, the supernatant was decanted. This procedure was repeated several times, till the supernatant was clear. The part of the powdered samples which had settled down was then washed with ethanol and filtered using a Buchner flask and a Whatman 589/3 filter paper (pore diameter < 2 μm). The filter residue was dried at 40 °C and used for further experimentation.

#### 2.1.1. Particle size distribution

The particle size distribution (PSD) of the starting Fe-powder was measured in isopropanol (IPA) as a suspension medium by laser diffraction (*Horiba LA-350*). Before the experiment was initiated, 200 mg to 400 mg of the powder sample was added to 20 mL IPA and the suspension was ultrasonicated for two minutes to disperse agglomerates. The ultrasonicated suspensions were measured in triplicate. Fig. 1 shows the percent volumetric distribution ($F_{i_0}$) of the powdered Fe-particles at representative diameters ($D_{i_0}$), as observed using the PSD analyzer. The particle size distribution is quite narrow with $D_{50}$ of 8 μm and $D_{90}$ of 13.5 μm.

*2.1.1.1. Total surface area using volume median diameter.* The rate of dissolution is usually represented by normalizing Fe-concentrations in the solutions to the duration of the dissolution and the initial specific surface area [24]. Equation (1) uses the volumetric $D_{50}$ to calculate the geometric specific surface area ($A_{D_{v,50}}$). Here $D_{v,50}$ is the volume-based median particle size of the powder of an assumed spherical particle. The $A_{D_{v,50}}$ was calculated to be 0.092 $m^2/g$.

$$A_{D_{v,50}} = 4 \times \pi \times (D_{v,50}{}^2)/4 \tag{1}$$

*2.1.1.2. Total surface area using full particle size distribution.* Since the sample studied herein is a homogeneous powder, the volumetric distribution ($F_{i_0}$ in Fig. 1) at each $D_{i_0}$ can also be considered to represent mass distribution ($TM_{i_0}$). Here $TM_{i_0}$ represents the sum of masses of all the particles of each $D_{i_0}$ observed by the particle size analyzer. Assuming spherical particles, the surface areas ($A_{i_0}$), volumes ($V_{i_0}$), and masses

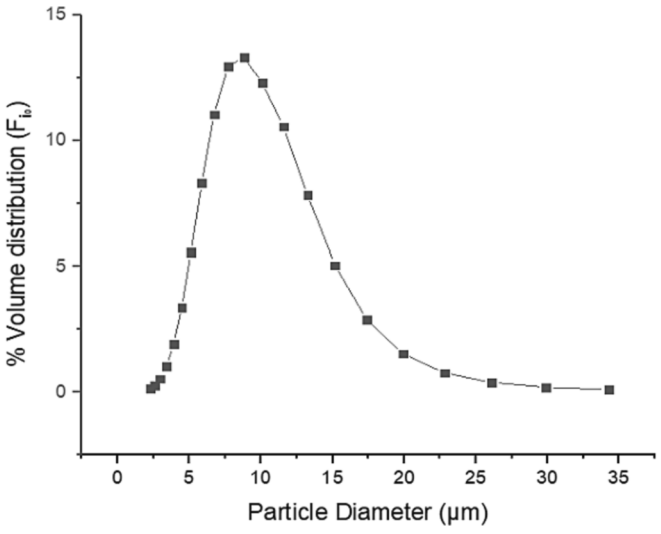


**Fig. 1.** Volumetric particle size distribution of Fe(0) sample.

($M_{i_0}$) of individual particles at each $D_{i_0}$ can be directly calculated. Furthermore, the number of particles ($P_i$) at each $D_{i_0}$ can be calculated as $TM_{i_0}/M_{i_0}$. Using these values, the 'total surface area at each $D_{i_0}$' ($TA_{i_0}$) can be calculated as their product ($TA_{i_0} = P_i \times A_{i_0}$). The calculated $TA_{i_0}$ for the powder sample was found to be 0.093 $m^2/g$, which is almost equivalent to $A_{D_{v,50}}$ of 0.092 $m^2/g$ calculated in the previous section. $TA_{i_0}$ is used for all the normalizations in this study.

### 2.2. Methods: Dissolution experiment

The dissolution experiments were performed using a stirred titanium batch reactor (Parr model A2230HC5EE) with a maximum volume of 0.450 L (Fig. 2). The study was performed at four combinations of temperature (T) and $CO_2$-pressures (P): (a) T = 30 °C, P = 1 barg (30C-1B), (b) T = 30 °C, P = 10 barg (30C-10B), (c) T = 60 °C, P = 1 barg (60C-1B), and (d) T = 60 °C, P = 10 barg (60C-10B).

For all the experiments, 400 mL of deionized water was introduced into the reactor and was preheated to the desired reaction temperature. For the benchmark studies involving pH-measurement of the $CO_2$-$H_2O$ systems without Fe(0), $CO_{2(g)}$ was thereafter introduced into the pre-heated water and the desired $CO_2$-pressure was maintained for 30 min. Subsequently, the pH of the $CO_2$-$H_2O$ benchmark systems was measured. For each reaction condition, the pH measurements for the $CO_2$-$H_2O$ benchmark systems were repeated three times, and the mean and standard deviations of these measurements are provided in Table 3.

For the systems involving studies on $CO_2$-induced Fe-dissolution, water was preheated to the desired temperature and thoroughly flushed with pressurized $CO_2$. Thereafter, 400 mg of Fe(0) powder sample was introduced into the reactor. The timer was started immediately after the introduction of the powder sample. The reactor was closed and flushed with $CO_{2(g)}$ for about two minutes at the desired $CO_2$-pressure. The whole process of closing and flushing after the introduction of the powder sample took about 4 min. Subsequently, the required $CO_2$-pressure was applied and maintained throughout the experiment. In the reactor, stirring was performed at 400 rpm throughout the experiment.

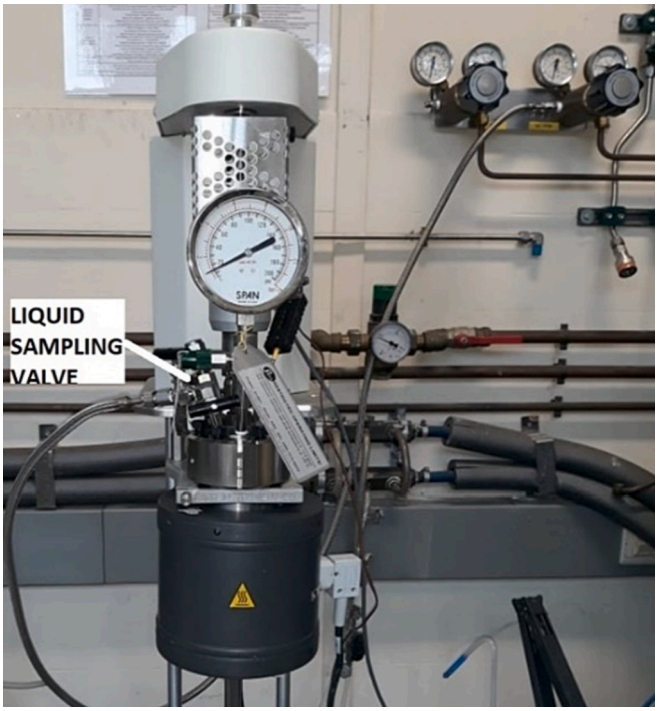


**Fig. 2.** Parr model A2230HC5EE reactor used for this study (with the location of sampling valve) available at the Flemish Institute for Technological Research (VITO).

The samplings were performed at 30, 60, 120, and 240 min from the initiation of the experiment. The maximum duration of the experiments is limited to 4 h since earlier studies have found this time to be sufficient for a significant degree of reaction within the reaction conditions studied in this work [4-6,10]. For sampling, the reactor has a typical liquid sampling valve (Fig. 2) the inlet of which is connected to a sampling dip tube. To collect the liquid samples, a 20 mL plastic syringe was prepared by fitting the nozzle of the syringe with a disposable polypropylene syringe filter (Chromafil AO-45/25, Macherey-Nagel, pore diameter of 0.45 μm). At the stipulated time, about 14 mL of liquid sample was recovered through the sampling valve and immediately filtered. Of the 14 mL solution, about 4 mL of the solution was filtered into a sampling tube that was fitted with a pH meter to initiate measurement of the solution pH within one minute from the time of removal of the samples from the pressure/temperature reactor. The other 10 mL was injected in a separate tube for analysis of the concentration of the dissolved-Fe using inductively coupled plasma atomic emission spectroscopy (ICP-AES instrument available at VITO) as described in section 2.2.2.

As a benchmark study, Fe-dissolution in pressurized $N_{2(g)}$ atmosphere was also investigated to quantify the influence of pressurized water without $CO_{2(g)}$ on Fe-dissolution.

#### 2.2.1. pH measurement

The pH of the filtered solutions was measured using a Mettler Toledo instrument. The instrument was calibrated every day using buffers of pH 2, 4.01, 7.00, 9.21, and 11. All the pH measurements were temperature corrected. It is noted that there are several possible sources of error in pH measurement due to the limitations of the setup used in this study. In particular, the pH of the solutions was measured after taking the solution out of the pressurized/temperature reactor. To minimize the error due to the escape of hydrated-$CO_2$, efforts were made to measure the solution-pH within < 1 min after being removed from the reactor. This ensured that the temperature was within 5 of the in-situ temperature at which the experiments were performed. To indicate the possible magnitude of error in pH measurement, comparisons are shown in section 2.7.2 (Table 3) between the pH calculated using a chemical modeling approach utilized in this study, and the experimentally measured pH for the benchmark $CO_2$-$H_2O$ systems studied in this work.

#### 2.2.2. Elemental composition of filtered solutions

The concentrations of the dissolved-Fe in the filtered solutions were determined using ICP-AES (PerkinElmer Avio 500). The detection limit for Fe in the non-diluted solution using the instrument was 5 μg/l. For the storage of the filtered solutions after being removed from the reactor, 10 mL of the filtered solution was added with 0.5 mL of $HNO_3$ (Fisher Scientific, optima grade, 67–69% assay). Subsequently, ICP-AES analyses were performed on each of these solutions.

#### 2.2.3. Rate of Fe-dissolution ($R_{\Delta t,TA_{i_0}}$, in mol/s/$m^2$)

To measure the respective activation energies, the rates of Fe-dissolution ($R_{\Delta t,TA_{i_0}}$) are calculated for all the systems using Equation (3), where Δ[Fe] represents the change in solution Fe-concentrations in Δ$t$ seconds [25]. The $TA_{i_0}$ is the total initial surface area calculated using the particle size distribution (section 2.2.2).

$$R_{\Delta t,TA_{i_0}} = \frac{\Delta[\mathrm{Fe}]}{(\Delta t) \times TA_{i_0}} \tag{3}$$

### 2.3. Methods: Chemistry modeling approach and comparison with the $CO_2$-$H_2O$

The composition of the bulk solution in which Fe(0) dissolves is an important determinant of how Fe(0) behaves in a given $CO_{2(g)}$–$H_2O$-Fe system. In this context, the process conditions such as temperature and $CO_2$-pressure can have a significant influence.

The solution chemistries of the $CO_2$-$H_2O$ and different $CO_2$-$H_2O$-Fe systems were modeled using well-established empirical correlations of chemical equilibria from literature. The reactions considered for this model are listed in Table 1 as compiled previously by [26]. Square brackets are used to denote the molarity, rather than activity, of a species for each reaction as non-idealities related to system pressure and ionic strength are accounted for within the empirical formulae derived for each equilibrium constant provided in Table 2. The same approach is taken for $CO_2$ solubility where partial pressure is used in place of fugacity.

With five reaction equations containing unknown concentrations for six different species (Table 2), a sixth equation (Equation (9)) [27] in the form of a charge balance is commonly used to resolve the system speciation.

$$[H^+] + 2[Fe^{2+}] - [OH^-] - [HCO_3^-] - 2[CO_3^{2-}] = 0 \quad (9)$$

The charge balance equation includes concentrations for each cationic and anionic species, including dissolved $Fe^{2+}$ as a result of the anodic reaction (Reaction 6). By substituting the formulae in Table 2 into the charge neutrality equation and re-arranging in terms of $[H^+]$, the following cubic equation (Equation (10)) is derived [27]:

$$\mathbb{C}_1[H^+]^3 + \mathbb{C}_2[H^+]^2 + \mathbb{C}_3[H^+] + \mathbb{C}_4 = 0 \quad (10)$$

Where:

$\mathbb{C}_1 = 1$; $\mathbb{C}_2 = 2[Fe^{2+}]$; $\mathbb{C}_3 = -K_{wa} - K_{ca} \bullet K_{sol} \bullet pCO_2 \bullet K_{hy}$; $\mathbb{C}_4 = -2 \bullet K_{bi} \bullet (K_{wa} + \mathbb{C}_3)$

Resolving the cubic equation for a specified partial pressure of $CO_2$, temperature and $Fe^{2+}$ molarity will give the total $H^+$ concentration in the system. The remaining species concentrations are routinely solved by the application of the reaction equations from Table 2. The system speciation can be used to calculate ionic strength using the following equation (Equation (11)) [27]:

$$\mathbf{I} = \frac{1}{2}\sum_i c_i z_i^2 \quad (11)$$

Where $c_i$ is the concentration of the $i^{th}$ species in moles per liter and z is its corresponding charge. Given that the equilibrium constants are a function of ionic strength, an initial estimate of ionic strength must be made to provide a preliminary solution. The solution is subsequently refined through iterative computations until convergence is achieved (<0.1% change in results).

#### 2.3.1. Iron carbonate Saturation:

The degree of saturation for $FeCO_3$ is determined from the following equation (Equation (12)) [27]:

$$S = \frac{a_{Fe^{2+}} \times a_{CO_3^{2-}}}{K_{sp}} \quad (12)$$

where $a_{Fe^{2+}}$ and $a_{CO_3^{2-}}$ represent the activities of $Fe^{2+}$ and $CO_3^{2-}$ respectively. $K_{sp}$ is the solubility constant for $FeCO_3$. For this work the $K_{sp}$ correlation ((Equation (13)) derived by Sun and Nešić [31] has been adopted since it recognizes the contribution of ionic strength in the solubility formula:

$$\log(K_{sp}) = -59.3498 - 0.041377(T_k) - \frac{2.1963}{T_k} + 24.5724\log(T_k) + 2.518(\mathbf{I}^{0.5}) - 0.657(\mathbf{I}) \quad (13)$$

This equation also allows saturation ratio to be determined directly from molarities of $Fe^{2+}$ and $CO_3^{2-}$ as opposed to activities (Equation (12)). Moreover, it must be noted that the ionic strength (Equation (13)) affects the activity, and not $K_{sp}$ per se.

**Table 1**
Chemical reactions accounted for in $CO_2$ water chemistry model [27].

| Process | Reaction | Equilibrium Constant | |
|---|---|---|---|
| $CO_2$ dissolution | $CO_{2(g)} \rightleftharpoons CO_{2(aq)}$ | $K_{sol} = \frac{[CO_{2(aq)}]}{pCO_2}$ | Equation 4 |
| Water dissociation | $H_2O \rightleftharpoons H^+ + OH^-$ | $K_{wa} = [H^+][OH^-]$ | Equation 5 |
| $CO_2$ hydration | $CO_{2(aq)} + H_2O \rightleftharpoons H_2CO_3$ | $K_{hy} = \frac{[H_2CO_3]}{[CO_{2(aq)}]}$ | Equation 6 |
| Carbonic acid dissociation | $H_2CO_3 \rightleftharpoons H^+ + HCO_3^-$ | $K_{ca} = \frac{[H^+][HCO_3^-]}{[H_2CO_3]}$ | Equation 7 |
| Bicarbonate ion dissociation | $HCO_3^- \rightleftharpoons H^+ + CO_3^{2-}$ | $K_{bi} = \frac{[H^+][CO_3^{2-}]}{[HCO_3^-]}$ | Equation 8 |

## 3. Results and discussion

### 3.1. Benchmarking the $CO_2$-$H_2O$ systems (without Fe(0))

The modelled equilibrium compositions of $CO_2$-$H_2O$ systems, without Fe, are shown in Table 3 and are in line with earlier experimental and modeling results [32,33]. It can be observed from the table that at a given temperature, a 10x increase in $CO_2$-pressure from 1 to 10 barg leads to an approximate increase of $CO_2$-solubility by nearly 6x. It can further be observed that lowering the temperature from 60 to 30 °C at a given $CO_2$-pressure leads to an increase in $CO_2$-solubility by 1.6–1.75 times. The second to last column in the table shows the pH calculated using the chemistry modeling approach.

The last column in Table 3 exhibits the experimentally measured pH in the benchmark $CO_2$-$H_2O$ systems. For the experimental setup, it is noted that hydration of $CO_{2(aq)}$ is considered to be among the slowest steps in the $CO_2$ corrosion mechanism [34]. Therefore, to ensure that sufficient time was available to the $CO_2$-$H_2O$ systems to attain equilibrium, the time needed for hydration of $CO_{2(aq)}$ was calculated using the forward reaction rates ($k_{Hyd,\ fwd}$) (Equation (2)) [30,35]. The calculated reaction rates of 0.0369 $s^{-1}$ and 0.1474 $s^{-1}$ respectively for the systems at 30 °C and 60 °C indicate that these systems can reach equilibrium in about two minutes and half a minute, respectively. Therefore, it is safe to assume that the dissolution results, even for the first 30 min, are not influenced by the time taken by the $CO_2$-$H_2O$ systems to attain equilibrium. Other reactions in $CO_2$-$H_2O$ systems are known to be relatively fast [36].

$$k_{Hyd,\ fwd} = 10^{(329.85 - 110.541 \times \log T - \frac{17265.4}{T})} \quad (2)$$

From the comparison of the measured and the calculated solution-pH in the $CO_2$-$H_2O$ systems, the possible magnitude of the error introduced due to the setup can be appreciated. The experimental and the calculated values are comparable in the systems prepared at 1 barg $CO_2$-pressure. Among the systems prepared at 10 barg $CO_2$-pressure, the experimental values are slightly higher, which can be attributed to the relative pressure-loss due as the solutions are measured outside the reactor, as discussed in section 3.3.

### 3.2. Fe-dissolution with temperature and $CO_2$-pressure: Experimental observations

Fig. 3 exhibits the experimentally observed degrees of Fe-dissolution expressed as a percent of initial Fe masses over time as well as the mmol/L concentrations of Fe ([Fe]), in the studied Fe-$CO_2$-$H_2O$ systems. The Fe-dissolution in Fe-$N_{2(g)}$–$H_2O$ systems are used as benchmarks and are also shown in the figure. In the benchmark $N_2$ systems, the Fe-dissolution can be observed to be negligible during the entire study. Therefore, all the changes in the systems containing $CO_{2(g)}$ can be considered to have been affected by dissolved-$CO_2$.

#### 3.2.1. Influence of $CO_2$-pressures on Fe-dissolution

At a given temperature, the influence of $CO_2$-pressures on Fe-dissolution can be observed in Fig. 3. From the point of first

**Table 2**
List of chemical equilibrium constant equations from literature where $T_f$ is the temperature in Fahrenheit, $T_k$ is the temperature in Kelvin and p is total pressure.

| Equilibrium Constant Formula | Source |
|---|---|
| $K_{sol} = \frac{14.5}{1.00258} \times 10^{-\left(2.27+5.65\times10^{-3}\bullet T_f - 8.06\times10^{-6}\bullet T_f^2 + 0.075I\right)} \frac{molar}{bar}$ | [28] |
| $K_{wa} = 10^{-\left(29.3868-0.0737549\bullet T_k + 7.47881\times10^{-5}\bullet T_k^2\right)} molar^2$ | [29] |
| $K_{hy} = 2.58\times10^{-3}$ | [30] |
| $K_{ca} = 387.6\times10^{-\left(6.41-1.594\times10^{-3}\bullet T_f + 8.52\times10^{-6}\bullet T_f^2 - 3.07\times10^{-5}\bullet p - 0.4772\bullet I^{0.5} + 0.1180\bullet I\right)} molar$ | [28] |
| $K_{bi} = 10^{-\left(10.61-4.97\times10^{-3}\bullet T_f + 1.331\times10^{-5}\bullet T_f^2 - 2.624\times10^{-5}\bullet p - 1.166\bullet I^{0.5} + 0.3466\bullet I\right)} molar$ | [28] |

**Table 3**
Equilibrium speciation (mmol/L) and pH in $CO_2$-$H_2O$ system based on chemical modeling and experimental measurement (mean ± σ for 3 repetitions) (T: Temperature (°C); B: $CO_2$-pressure (barg)).

| | $[CO_{2(aq)}]$ | $[H_2CO_3]$ | $[HCO_3^-]$ | $[CO_3^{2-}]$ | $[H^+]$ | pH (Calculated) | pH (Experiment) |
|---|---|---|---|---|---|---|---|
| **30C-1B** | 5.74E-02 | 1.48E-04 | 1.64E-04 | 5.4E-11 | 1.64E-04 | 3.79 | 3.77 ± 0.05 |
| **30C-10B** | 3.19E-01 | 8.24E-04 | 3.88E-04 | 5.5E-11 | 3.88E-04 | 3.41 | 3.55 ± 0.03 |
| **60C-1B** | 3.28E-02 | 8.46E-05 | 1.21E-04 | 6.9E-11 | 1.21E-04 | 3.92 | 3.88 ± 0.06 |
| **60C-10B** | 1.96E-01 | 5.04E-04 | 2.97E-04 | 7E-11 | 2.97E-04 | 3.53 | 3.67 ± 0.03 |

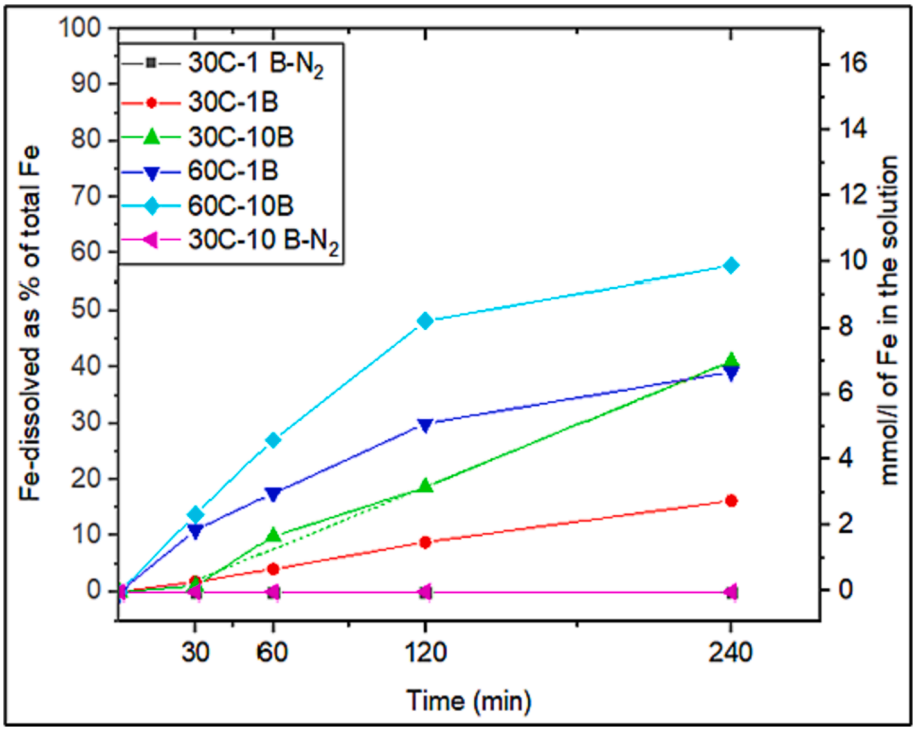


**Fig. 3.** Fe-dissolution as a function of $CO_2$-pressure, temperature, and duration.

observation at 30 min and onwards, among the systems at a given temperature, the systems at 10 barg $CO_2$-pressure exhibit higher degrees of Fe-dissolution compared to the systems at 1 barg $CO_2$-pressure (Fig. 3). The higher Fe-dissolution in the systems at higher $CO_2$-pressures is in line with the earlier observations that an increase in $CO_2$-pressure at a given temperature leads to a higher rate of $CO_2$-corrosion of Fe [37,38]. In general, this increase is attributed to higher $[H_2CO_3]$ and $[H^+]$ in the bulk $CO_2$-$H_2O$ systems, resulting from higher $CO_2$-solubility in the systems at higher $CO_2$-pressures [5,21]. Indeed, it can be observed from Table 3 that, at a given temperature, the $CO_2$-$H_2O$ systems at 10 barg $CO_2$-pressure have almost 6-times the $CO_2$-solubility compared to the systems at 1 barg. However, the data in the table does not show the evolution of the solution species ($CO_2$-species, $H^+$, and $OH^-$) as the [Fe] increases in the solution. As a side note, it is also interesting to mention that while the acidic species can also increase the solubility of $FeCO_3$, studies have found that the amounts of $FeCO_3$-binders usually remain higher at higher $CO_2$-pressure [5,6,39].

### 3.2.2. *Influence of process temperatures on Fe-dissolution*

At a given $CO_2$-pressure, the $CO_2$-$H_2O$ systems at 30 °C are expected to have almost twice the $CO_2$-solubilities compared to the systems at 60 °C (Table 3). It can further be observed from the table that this difference in $CO_2$-solubilities is manifested as lower pH in the $CO_2$-$H_2O$ systems at 30 °C compared to the systems at 60 °C. In the discussion of

the influence of $CO_2$-pressure, it was noted that the systems with higher $CO_2$-solubilities (i.e. higher $CO_2$-pressures) exhibited higher Fe-dissolution. However, as a function of temperature, the systems with higher $CO_2$-solubilities (i.e. lower temperature) exhibit lower Fe-dissolution. This shows that the degree of Fe-dissolution depends on the temperature increase simultaneously through two opposing mechanisms: (a) decreased availability of $[H^+]$ (or increased pH) due to decrease in $CO_2$-solubility, and (b) faster kinetics of interaction of the available $[H^+]$ with Fe(0) leading to faster Fe-dissolution. At the same time, the availability of $[H^+]$ is expected to decrease with an increase in $[Fe^{2+}]$, and one of the objectives of this study is to quantify the influence of this time-evolution in all the systems studied in this work.

During $FeCO_3$ scaling in ferrous pipelines, such interplaying influences of temperature are also observed during $CO_2$-corrosion in scale-free as well as scale-forming conditions [37,40]. In such studies, it is generally observed that at a given $CO_2$-pressure, the rate of $CO_2$-corrosion first increases with an increase in temperature (peaking at 50–90 °C), and then decreases with a further increase in temperature. According to the above-discussed explanation, as the process temperature is increased from 30 °C to 50–60 °C, the influence of temperature on Fe-dissolution kinetics dominates; however, with a further increase of temperature from 60 to 90 °C, the influence of temperature on kinetics is offset by its opposing influence on $CO_2$-solubility [4-6,10]. Similar observations were also made during the preparation of $FeCO_3$ cement by accelerated carbonation of Fe(0) at 30, 60, and 90 ℃ [5,6,10].

While this study focuses mainly on Fe-dissolution, the influence of temperature on $FeCO_3$-precipitation is also important to note. In the case of systems that were studied, a higher temperature is additionally expected to increase the rate of $FeCO_3$-precipitation. This can lead to: (a) reduction in the [Fe] in the solutions, and (b) precipitation of $FeCO_3$ as passivating scales at Fe-surfaces, leading to a reduction in the overall rate of Fe-dissolution by making the Fe-surfaces unavailable for further dissolution [31]. Because of such co-dependencies of Fe-dissolution and $FeCO_3$-precipitation on temperature, this study attempts to avoid $FeCO_3$-precipitation to understand the influence of temperature on Fe-dissolution. Within the range of temperatures and $CO_2$-pressure studied in this work, amounts of $FeCO_3$ cement are higher at higher temperatures indicating that the kinetics of Fe-dissolution dominate the amounts of product formation [4,5].

### 3.3. Evolution of systems with time and pH: Experimental and modeling results

$FeCO_3$-formation by direct aqueous carbonation of Fe(0) is a dissolution-precipitation process [21,27]. The rates of Fe-dissolution and $FeCO_3$-precipitation are known to be dependent on their environment: as the [Fe] in the solutions increases, the accompanying changes in the solution composition (increase in pH, $CO_3^{2-}$, $HCO_3^-$) can decrease the rate of Fe-dissolution and increase the rate of $FeCO_3$-precipitation [31,39]. The plots in Fig. 4 show the modeled $[H^+]$, $[HCO_3^-]$, $[OH^-]$, $[CO_3^{2-}]$, $[CO_{2(aq)}]$, and $[H_2CO_3]$. In all the conditions, the trends of decreasing $[H^+]$ with an increase in $[Fe^{2+}]$ can be observed. At the same time, an increase in $[HCO_3^-]$, $[OH^-]$, and $[CO_3^{2-}]$ with increase in $[Fe^{2+}]$ can also be observed. The $[CO_{2(aq)}]$ and $[H_2CO_3]$ remain undisturbed, as expected [30]. By plugging in the experimentally observed $[Fe^{2+}]$ in these correlations, the concentrations of the dependent species and the modeled pH are calculated later in this discussion (Fig. 5).

Fig. 5(a) shows the experimentally observed increase in solution pH with the increase in the [Fe]. In the figure, the values at 0 min exhibit the pH in the $CO_2$-$H_2O$ systems without Fe(0). Moreover, the dotted lines are the best-fit lines for the observations between 0 and 30 min, and the solid lines are the best-fit lines for the four observations made at 30, 60, 120, and 240 min. The modeled relationship between the solution pH and $[Fe^{2+}]$ in the studied systems is shown in Fig. 5(b). In Fig. 5(a) and Fig. 5(b), pH on the y-axes exhibits $[H^+]$ on a logarithmic scale: there appears to be a linear relationship between [Fe] and pH in all the cases.

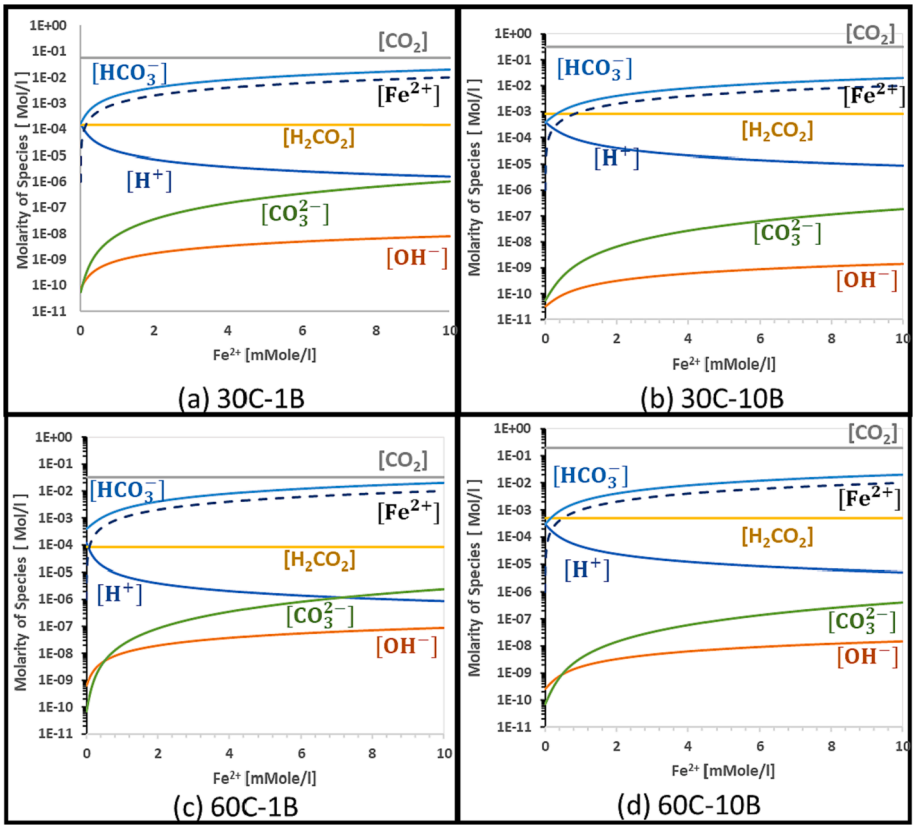


**Fig. 4.** Modeled $[H^+]$, $[HCO_3^-]$, $[OH^-]$, $[CO_3^{2-}]$, $[CO_{2(aq)}]$, and $[H_2CO_3]$ as function of $[Fe^{2+}]$ in the systems at (a) 30C-1B, (b) 30C-10B, (c) 60C-1B, (d) 60C-10B.

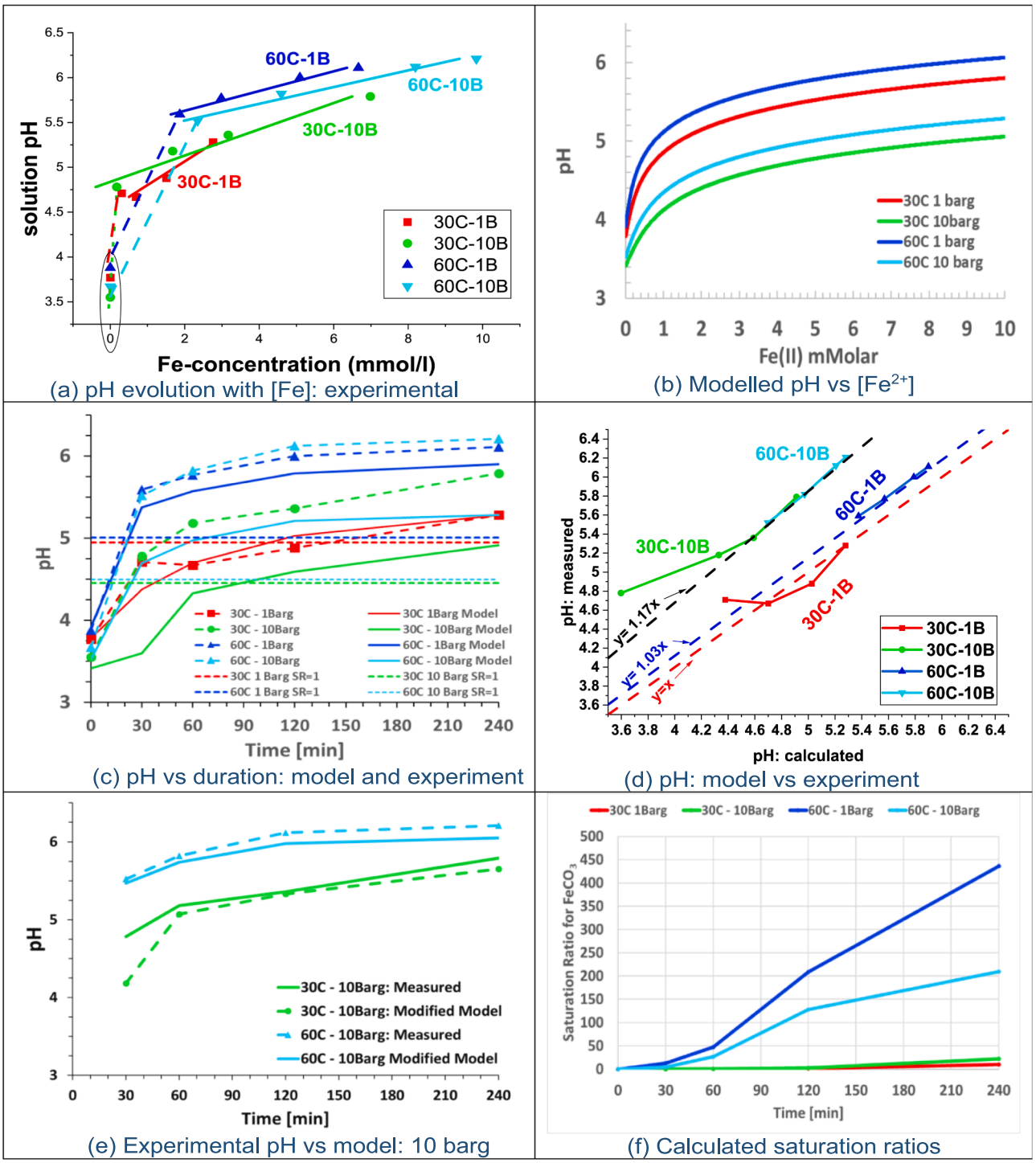


**Fig. 5.** (a) Experimentally observed solution-pH as functions of [Fe] in the solutions (value at 0 min are those observed in $CO_2$-$H_2O$ systems) (b) pH vs [Fe] based on modeling, (c) comparison of pH evolution as a function of time (modeling vs experimental), where dotted lines parallel to x-axis denote pH when saturation ratios = 1, (d) measured vs calculated pH, (e) comparison of measured pH (dotted) with modified modeled, calculated by assuming $CO_2$-pressure of 1 barg during calculation (f) Calculated $FeCO_3$ saturation ratios based on modeling results.

In Fig. 5(b), it can be observed that at a given temperature and [Fe], the systems at higher $CO_2$-pressure exhibit lower pH. At the same time, at a given $CO_2$-pressure and [Fe], the systems at lower temperatures exhibit lower pH. Such lower pH at a given [Fe] can be attributed to higher $CO_2$-solubility at higher $CO_2$-pressures and lower temperatures [5]. This study is performed as a function of time: the experimentally observed [Fe] at 30, 60, 120, and 240 min are plugged in Fig. 5(b) to attain the modelled-pH at the relevant points in time.

The increase in the solution-pH over time can be observed from Fig. 5 (c), which shows the comparison of the experimental and modeled time-evolution of pH. The experimental and the modeled systems at 1 barg appear to be in relatively good agreement, while there are disagreements at 10 barg. This can be observed more clearly from the correlations between experimental and modeled pH in Fig. 5(d). The figure also contains three functional lines at: (a) y = x, (b) y = 1.03x, and (c) y = 1.17x. In the figure, the agreement between the experimental and

modeled values in the systems at 1 barg $CO_2$-pressure can be observed from the proximity of the plotted points to y = x. Interestingly, most of the data points in the systems prepared at 10 barg $CO_2$-pressure lie near the y = 1.17x line, exhibiting lower modeled-pH than experimental. Moreover, in the experimental results, the systems at 10 barg $CO_2$-pressure exhibited higher pH than those at 1 barg $CO_2$-pressure in almost all the observations. On the other hand, based on the modeling data, the systems at 10 barg continuously exhibit significantly lower pH than the systems at 1 barg.

The observed disagreement between experimental and modeling results can be attributed to the differences in their *apparent* sampling procedures: while the modeling values represent in-situ conditions, the experimental values are observed by bringing the samples outside the reactor before being filtered and tested for their [Fe] and pH. Based on this experimental limitation, two causes for the observed disagreement can be conjectured: (a) increase in the actual solution pH due to $CO_2$-depressurization, and (b) precipitation of dissolved-Fe leading to lower *experimentally observed [Fe]*, which can in-turn exhibit lower modeled pH since the increase in the modeled pH is caused by the increase in experimentally observed [Fe] in Fig. 5(b). Both the cases would have different implications: while the former would mean that the ***experimental pH*** in the systems at 10 barg is overvalued due to the loss of dissolved-$CO_2$, the latter would mean that the ***modeled pH*** in the 10 barg systems is undervalued due to the precipitation of dissolved-Fe before the filtration of the solution.

It is interesting to explore the validity of the first conjecture by (theoretically) assuming that there was no Fe-precipitation due to the depressurization and that the higher experimental pH solely represents the reduction in the dissolved-$CO_2$ species due to depressurization. Under this assumption, when the [Fe] in the 10 barg systems were plugged into the curves corresponding to 1 barg $CO_2$-pressure at a given temperature, the *modified modeled* pH-vs time curves for the 10 barg systems are shown in Fig. 5(e). In the figure, the *modified modeled* pH shows quite a good agreement with the experimental values. Therefore, the reduction in the $[H^+]$ due to the loss of dissolved-$CO_2$ during the depressurization could have a significant influence on the disagreement observed in Fig. 5(c).

The scope of this study is limited by the assumption that there was negligible precipitation of dissolved Fe. For this, attempts were made to minimize the precipitation of dissolved-Fe by using a relatively high l/s (w/w) of 1000. Moreover, a high stirring rate of 400 RPM was used to reduce the precipitation rates at any saturation ratio (SR) [41,42]. At combinations of such high dilution and high stirring rates, even if the SRs are thermodynamically favorable for the precipitation of dissolved-Fe, the nucleation events can be very slow leading to relatively high induction periods of several days, compared to the 4 h for which the systems were studied in this work [21]. However, it is worthwhile to evaluate the second conjecture regarding the role of Fe-precipitation during the experiment or sampling as a cause for the disagreement in the 10 barg systems (Fig. 5(d)).

Since the modeled-pH in Fig. 5(c) is calculated by plugging in the experimentally observed [Fe] in Fig. 5(b), lowering of experimental [Fe] can indeed explain the lower modeled pH compared to the measured pH in the 10 barg systems. To evaluate this, the saturation ratios (SR) of $FeCO_3$ (calculations in section 2.7.1) are plotted at each point of observation in Fig. 5(f). Among the systems at 60 ℃, the SRs are significantly and continuously higher in the 1 barg systems (~12.5 in 30 min, to ~ 450 in 240 min) compared to the 10 barg systems (~4 in 30 min to ~ 210 in 240 min). Therefore, theoretically, if $FeCO_3$ precipitation were solely the cause for the disagreement, then the disagreements should have been much higher at 1 barg. This is contrary to the observations made in this study. Among the systems at 30 ℃, while the SRs in the 10 barg systems are higher, the corresponding values are only 0.002 (30 min), 0.426 (60 min), 2.54 (120 min), and 22.4 (240 min). Therefore, the disagreement in the 30 ℃, at least for the first 120 min, is difficult to explain through $FeCO_3$-precipitation.

Studying the time-evolution of solution compositions in high-pressure systems is complicated and requires high-precision and specialized instruments. Therefore, developing correlations between pressurized and non-pressurized systems, as in this study, could be highly beneficial for future studies in which pH and/or [Fe] cannot be measured in-situ in high-pressure vessels.

### 3.4. Understanding the dissolution kinetics

While pH plays a vital role in Fe-dissolution, this study reiterates the importance influence of reaction conditions on dissolution kinetics. Indeed, from the modeled-pH in Fig. 5(c) and the corresponding $[H^+]$ in Fig. 6(a), it can be observed that, at a given $CO_2$-pressure, the systems at 30 °C continuously exhibit higher $[H^+]$ than the systems at 60 °C, throughout the 240 min of the study. However, such persistently higher $[H^+]$ in the systems prepared at 30 °C does not materialize into an increase in Fe-dissolution in such systems compared to the systems prepared at 60 °C (Fig. 3). This can be observed from the evolution of the dissolution rates calculated using Equation (3) and shown in Fig. 6(b). In the figure, it can be observed that the systems at lower temperatures exhibit lower dissolution rates, even if their $[H^+]$ is higher. In general, it can be observed that the rate of dissolution decreases with time in each system, as expected due to the increase in [Fe] and pH. The decrease in dissolution rate appears to be relatively stable between 30 and 120 min in both the systems at 60 °C and between 60 and 240 min in the systems prepared at 30℃. Therefore, the representative rates of dissolution are calculated by using best-fit lines between these data points and are shown as solid lines in Fig. 6(b). The respective rates of dissolution ($R_{\Delta t,TA_{i_0}}$, *in mol/s/m²*) were found to be: (a) 30C-1B: $2.62 \times 10^{-6}$, (b) 30C-10B: $7.95 \times 10^{-6}$, (c) 60C-1B: $11.4 \times 10^{-6}$, and (d) 60C-10B: $15.7 \times 10^{-6}$.

For a better understanding of the dissolution kinetics, activation energies are also calculated using the above-calculated dissolution rates. The activation energies at 1 barg and 10 barg $CO_2$-pressure were calculated using an Arrhenius plot by plotting the natural logarithm of the reaction rates as a function of $-1/RT$ (Fig. 6(c)). The respective activation energies were found to be 21.5 kJ/mol for the systems 10 barg $CO_2$-pressure and 32 kJ/mol for the systems at 1 barg $CO_2$-pressure. Similar to this, in a recent study on the dissolution of 3–5 μm Fe-particles for $H_2$-production under ~ 1 barg starting $CO_2$-pressure, the activation energy was calculated to be ~ 31 kJ/mol [43]. The activation energy for Fe-dissolution in strong acids has been noted to be ~ 60 kJ/mol [43]. Therefore, at 1 barg and 10 barg $CO_2$-pressures, the activation energies are respectively half and one-third of those observed in strong acids. In this context, it is well-established that $CO_2$-induced reduction in pH is more corrosive for Fe compared to the equivalent lowering of pH achieved using strong acids, possibly explaining the relatively low activation energies [15,37,44,45]. The relatively higher corrosivity of dissolved-$CO_2$ (compared to strong acids) has mainly been attributed to $H_2CO_3$, either through its role to buffer $[H^+]$, or by its direct reduction [46,47]. It has also been proposed that the complexation mechanism for $CO_2$-induced Fe-dissolution is different from the complexation mechanism known for strong acids [21,48], while others have suggested that the observed variation is based on the difference in the reaction conditions [49].

Fe-dissolution in $CO_2$-environment includes several processes: (a) $CO_2$-$H_2O$ interaction and $CO_2$-speciation (including $H^+$), (b) transport of the species to and from the Fe-surfaces into the bulk, (c) interaction of the dissolved $CO_2$-species with the Fe-surfaces. Among these, the slow hydration of $CO_{2(aq)}$ to $H_2CO_3$ has often been considered as one of the possible rate-limiting steps [34]. However, the higher l/s ratio of ~ 1000 used in this study can reduce the influence of this slow $CO_2$-hydration by keeping sufficient $H_2CO_3$ available in the bulk solution. Additionally, while the influence of transport control needs to be considered, the high stirring rate of 400 RPM is expected to compensate for this influence to a

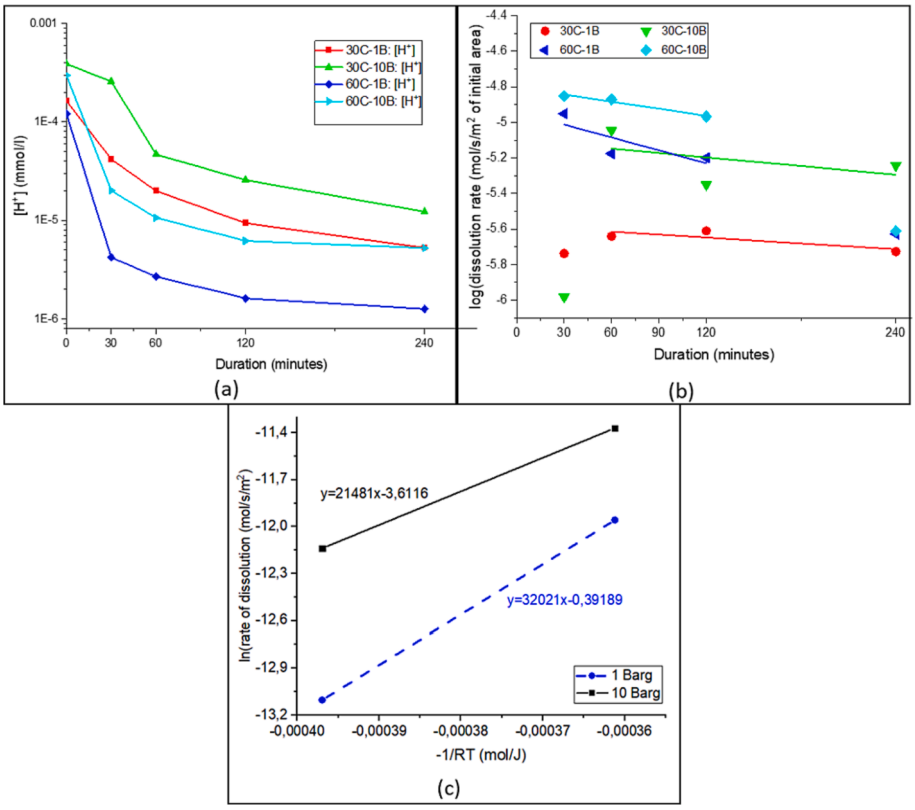


**Fig. 6.** (a) evolution of $[H^+]$ as a function of temperature, $CO_2$-pressure, and duration, (b) dissolution rate between each time interval, and best fit lines for the systems at 60℃ (for data 30–120 min) and 30 ℃ (for data 60–240 min) (c) Arrhenius plots of the systems at 1 and 10 barg $CO_2$-pressure.

large extent. At the same time, the low activation energies (Fig. 6(c)) may also be indicative of surface chemical reactions being the rate-limiting processes.

## 4. Conclusions

To understand the influence of reaction conditions on Fe-dissolution, a setup with a high l/s ratio and a high stirring speed was used in this study to avoid the precipitation of the dissolved-Fe. It is observed that an increase in temperature and $CO_2$-pressure leads to higher Fe-dissolutions (Fig. 3). Additionally, it is experimentally observed that the increase in [Fe] is accompanied by an increase in solution-pH (Fig. 5 (a)). A modeling approach is developed to calculate the evolution of $[H^+]$, $[HCO_3^-]$, $[OH^-]$, $[CO_3^{2-}]$, $[CO_{2(aq)}]$, and $[H_2CO_3]$ with increase in [Fe]. Based on these, the solution pH is calculated for each point of observation. The experimentally observed and modeled pH are found to be comparable in the systems prepared at 1 barg $CO_2$-pressure, and the systems at 10 barg showed ~ 1.2 times higher pH than predicted using modeling (irrespective of the temperature) (Fig. 5(c, d, e)). Two causes for this difference in the systems prepared at 10 barg are theoretically discussed: (a) decreased in acidic species due to $CO_2$-depressurization leading to increase in *experimentally observed* solution pH, and (b) precipitation of dissolved-Fe during the experiment or during sampling leading to lower modeled pH as higher experimentally observed [Fe] is expected to give higher *modeled pH*. Based on the discussion, the former reason appears to be more appropriate, but detailed studies are still needed. It is proposed that future studies could develop a correlation between the pH in pressurized and non-pressurized $CO_2$-$H_2O$ systems since the determination of pH under high $CO_2$-pressures is technically challenging.

The activation energies for $CO_2$-induced Fe-dissolution are found to be one-third (at 10 barg $CO_2$-pressure) and a half (at 1 barg $CO_2$-pressure) of those known for stronger acids. This observation is attributed to the higher corrosivity of dissolved-$CO_2$ at a given pH (compared to the stronger acids) due to the high amounts of $CO_{2(aq)}$ which acts as a buffer for the acidic species as they are consumed during Fe-dissolution.

## 5. Data availability statement

The raw/processed data required to reproduce these findings cannot be shared at this time due to technical or time limitations.

## Funding

The authors wish to acknowledge the Province of Antwerp for research funding (Research project no. 33466).

### *CRediT authorship contribution statement*

**Sumit Srivastava:** Conceptualization, Methodology, Validation, Formal analysis, Investigation, Writing – original draft, Writing – review & editing, Visualization, Funding acquisition. **Rob Jacklin:** Formal analysis, Investigation, Writing – original draft, Visualization. **Ruben Snellings:** Supervision, Resources, Conceptualization, Methodology, Validation, Writing – review & editing, Project administration, Funding acquisition. **Richard Barker:** Writing – review & editing. **Jeroen Spooren:** Writing – review & editing. **Pegie Cool:** Supervision, Resources, Writing – review & editing, Project administration, Funding acquisition.

## Declaration of Competing Interest

The authors declare that they have no known competing financial interests or personal relationships that could have appeared to influence the work reported in this paper.

## Data availability

Data will be made available on request.

## Acknowledgment

The authors wish to thank Miss Julie Verlinde for performing the experiments as planned. The authors also wish to thank Prof. Vera Meynen, Prof. Tom Breugelmans, Prof. Ozlem Cizer, and Prof. Paivo Kinnunen for the discussions and suggestions. The authors also wish to acknowledge the technical support by Mr. Bo Peeraer for his help with the general experimental setup and execution.

## References

[1] S. Das, B. Souliman, D. Stone, N. Neithalath, Synthesis and properties of a novel structural binder utilizing the chemistry of iron carbonation, ACS Appl. Mater. Interfaces 6 (11) (2014) 8295–8304, https://doi.org/10.1021/am5011145.
[2] S. Das, A. Hendrix, D. Stone, N. Neithalath, Flexural fracture response of a novel iron carbonate matrix – Glass fiber composite and its comparison to Portland cement-based composites, Constr. Build. Mater. 93 (15) (2015) 360–370, https://doi.org/10.1016/j.conbuildmat.2015.06.011.
[3] S. Das, D. Stone, B. Mobasher, N. Neithalath, Strain energy and process zone based fracture characterization of a novel iron carbonate binding material, Engineering Fracture Mechanics. 156 (2016) 1–15.
[4] S. Srivastava, Towards co-utilization of CO2 and Fe-rich sources to prepare clinker-free carbonate-bonded monoliths, in Department of Chemistry, University of Antwerp, Antwerp, 2021 https://hdl.handle.net/10067/1755970151162165141.
[5] S. Srivastava, R. Snellings, V. Meynen, P. Cool, Utilising the principles of FeCO3 scaling for cementation in H2O-CO2(g)-Fe system, Corrosion Science. 169 (2020), 108613, https://doi.org/10.1016/j.corsci.2020.108613.
[6] S. Srivastava, R. Snellings, V. Meynen, P. Cool, Siderite-calcite (FeCO3–CaCO3) series cement formation by accelerated carbonation of CO2(g)–H2O–Fe–Ca(OH)2 systems, Cement and Concrete Composites. 122 (2021), 104137, https://doi.org/10.1016/j.cemconcomp.2021.104137.
[7] D.S. Vijayan, S. Dineshkumar, T.S. Arvindan, Janarthanan,, Evaluation of ferrock: A greener substitute to cement, Materials Today: Proceedings. 22 (3) (2020) 781–787, https://doi.org/10.1016/j.matpr.2019.10.147.
[8] S. Srivastava, R. Snellings, V. Meynen, P. Cool, (FeCO3) cementation by carbonation of iron rich systems, SSRN Electronic J. (2019), https://doi.org/10.2139/ssrn.3902662.
[9] S. Srivastava, R. Snellings, P. Cool, Clinker-free carbonate-bonded (CFCB) products prepared by accelerated carbonation of steel furnace slags: A parametric overview of the process development, Construction and Building Materials 303 (2021) 124556.
[10] S. Srivastava, Quaghebeur Mieke, R. Snellings, Method of producing a metal carbonate bonded article and carbonate bonded article, US Patent application WO2019234066A1, 2019.
[11] D. Stone, Curable composition, paste, and oxidatively carbonated composition, US patent US8366820B2 (2006).
[12] N. Neithalath, D. Stone, Binder Compositions and Method of Synthesis, US patent US20160075603A1 (2014).
[13] Ironkast.com, Http://Ironkast.Com/Wp-Content/Uploads/2017/11/USC-Ferrock-Final-Paper-4.24.17.Pdf (Accessed Oct. 2021). (2021).
[14] M.B. Kermani, A. Morshed, Carbon dioxide corrosion in oil and gas production—A compendium, Corrosion 59 (8) (2003) 659–683, https://doi.org/10.5006/1.3277596.
[15] A. Kahyarian M. Achour S. Nesic Mathematical modeling of uniform CO 2 corrosion Trends in Oil and Gas Corrosion Research and Technologies 2017 Elsevier p. 805 849, 10.1016/B978-0-08-101105-8.00034-6.
[16] Mohd F. Mohamed, Azmi M. Nor, Muhammad F. Suhor, Marc Singer, Yoon Seok Choi, Srdjan Nešic, Water chemistry for corrosion prediction in high pressure CO2 environments. In CORROSION 2011 Mar 13. OnePetro.
[17] P. Marcus Corrosion Mechanisms in Theory and Practice 0 CRC Press.
[18] A. Kahyarian, B. Brown, S. Nesic, Mechanism of CO2 corrosion of mild steel: A new narrative, in: CORROSION 2018, NACE-2018-11232, Phoenix, Arizona, USA, 2018.
[19] A. Kahyarian, B. Brown, S. Nešić, Technical note: electrochemistry of CO2 corrosion of mild steel: effect of CO2 on cathodic currents, Corrosion 74 (8) (2018) 851–859, https://doi.org/10.5006/2792.
[20] A. Kahyarian, B. Brown, S. Nesic, Electrochemistry of CO 2 corrosion of mild steel: Effect of CO 2 on iron dissolution reaction, Corrosion Science 129 (2017) 146–151.
[21] R. Barker, D. Burkle, T. Charpentier, H. Thompson, A. Neville, A review of iron carbonate (FeCO3) formation in the oil and gas industry, Corrosion Science 142 (2018) 312–341.
[22] S. Das, D. Stone, D. Convey, N. Neithalath, Pore- and micro-structural characterization of a novel structural binder based on iron carbonation, Materials Characterization 98 (2014) 168–179.
[23] C. De waard, D.E. Milliams, Carbonic acid corrosion of steel, Corrosion 31 (5) (1975) 177–181.
[24] R. Snellings, C. Jantzen, Solution-controlled dissolution of supplementary cementitious material glasses at pH 13: the effect of solution composition on glass dissolution rates, J. Am. Ceramic Society. 96 (8) (2013) 2467–2475.
[25] S. Srivastava, R. Snellings, P. Nielsen, P. Cool, Insights into CO2-mineralization using non-ferrous metallurgy slags: CO2(g)-induced dissolution behavior of copper and lead slags, J. Environ. Chem. Eng. 10 (2) (2022) 107338.
[26] M. Nordsveen, S. Nešić, R. Nyborg, A. Stangeland, A Mechanistic Model for Carbon Dioxide Corrosion of Mild Steel in the Presence of Protective Iron Carbonate Films—Part 1: Theory and Verification, Corrosion. 59 (5) (2003) 443–456, https://doi.org/10.5006/1.3277576.
[27] A. Kahyarian, M. Singer, S. Nesic, Modeling of uniform CO2 corrosion of mild steel in gas transportation systems: A review, J. Nat. Gas Sci. Eng. 29 (2016) 530–549, https://doi.org/10.1016/j.jngse.2015.12.052.
[28] J.E. Oddo, M.B. Tomson, Simplified calculation of CACO3 saturation at high temperatures and pressures in brine solutions, J. Petroleum Technology. 34 (07) (1982) (1590.) 1583, https://doi.org/10.2118/10352-PA.
[29] E.H. Perkins Y.K. Kharaka W.D. Gunter J.D. DeBraal 117 127.
[30] D.A. Palmer, R. Van Eldik, The chemistry of metal carbonato and carbon dioxide complexes, Chem. Rev. 83 (6) (1983) 651–731.
[31] W. Sun, S. Nešić, R.C. Woollam, The effect of temperature and ionic strength on iron carbonate (FeCO3) solubility limit, Corrosion Science 51 (6) (2009) 1273–1276.
[32] R.K. Haghi, A. Chapoy, L.M.C. Peirera, J. Yang, B. Tohidi, pH of CO 2 saturated water and CO 2 saturated brines: Experimental measurements and modelling, Int. J. Greenhouse Gas Control 66 (2017) 190–203.
[33] C. de Waard, U. Lotz, D.E. Milliams, Predictive model for CO 2 corrosion engineering in wet natural gas pipelines, Corrosion. 47 (12) (1991) 976–985, https://doi.org/10.5006/1.3585212.
[34] A. Kahyarian, A. Schumaker, B. Brown, S. Nesic, Acidic corrosion of mild steel in the presence of acetic acid: Mechanism and prediction, Electrochimica Acta 258 (2017) 639–652.
[35] L.C. Garg, T.H. Maren, The rates of hydration of carbon dioxide and dehydration of carbonic acid at 37°, Biochimica et Biophysica Acta (BBA) - General Subjects 261 (1) (1972) 70–76.
[36] R. E. Zeebe, D. W. Gladrow, Chapter 2 Kinetics, in: Elsevier Oceanography Series, 65 (2001), p: 85 140. https://doi.org/10.1016/S0422-9894(01)80003-9.
[37] S. Nešić, Key issues related to modelling of internal corrosion of oil and gas pipelines – A review, Corrosion Science. 49 (12) (2007) 85–140, https://doi.org/10.1016/j.corsci.2007.06.006.
[38] Y. Sun, S. Nesic, A parametric study and modeling on localized CO2 corrosion in horizontal wet gas flow, in: CORROSION 2004, NACE-04380, New Orleans, Louisiana, 2004.
[39] P.L. Fosbøl, K. Thomsen, E.H. Stenby, Review and recommended thermodynamic properties of FeCO 3, Corrosion Engineering, Science and Technology 45 (2) (2010) 115–135.
[40] R. Elgaddafi, A. Naidu, R. Ahmed, S. Shah, S. Hassani, S.O. Osisanya, A. Saasen, Modeling and experimental study of CO2 corrosion on carbon steel at elevated pressure and temperature, Journal of Natural Gas Science and Engineering 27 (2015) 1620–1629.
[41] D.P., Burkle, Understanding the Formation of Protective FeCO3 on to Carbon Steel Pipelines during CO2 Corrosion Ph.D. thesis 2017 https://etheses.whiterose.ac.uk/17608/.
[42] M.H. Sk, A.M. Abdullah, M. Ko, B. Ingham, N. Laycock, R. Arul, D.E. Williams, Local supersaturation and the growth of protective scales during CO2 corrosion of steel: Effect of pH and solution flow, Corrosion Science 126 (2017) 26–36.
[43] H. Eba, M. Takahashi, K. Sakurai, Progress of hydrogen gas generation by reaction between iron and steel powder and carbonate water in the temperature range near room temperature, International Journal of Hydrogen Energy. 45 (27) (2020) 13832–13840, https://doi.org/10.1016/j.ijhydene.2020.03.087.
[44] I. Matsushima, Carbon Steel-Corrosion in Freshwaters, in: Uhlig's Corrosion Handbook, (2011), pp.589 600 John Wiley & Sons, Inc., Hoboken, NJ, USA. https://doi.org/10.1002/9780470872864.ch44.
[45] G.W. Whitman, R.P. Russell, V.J. Altieri, Effect of hydrogen-ion concentration on the submerged corrosion of steel, Industrial & Engineering Chemistry. 16 (7) (1924) 589–600, https://doi.org/10.1021/ie50175a002.
[46] E. Remita, B. Tribollet, E. Sutter, V. Vivier, F. Ropital, J. Kittel, Hydrogen evolution in aqueous solutions containing dissolved CO2: Quantitative contribution of the buffering effect, Corrosion Science 50 (5) (2008) 1433–1440.
[47] T. Tran, B. Brown, S. Nesic, Corrosion of mild steel in an aqueous CO2 environment–basic electrochemical mechanisms revisited, in: Corrosion 2015, NACE-2015-5671, Dallas, Texas, 2015.
[48] S. Nesic, J. Postlethwaite, S. Olsen, An electrochemical model for prediction of corrosion of mild steel in aqueous carbon dioxide solutions, CORROSION. 52 (4) (1996) 280 294, https://doi.org/10.5006/1.3293640.
[49] T. das Chagas Almeida, M.C.E. Bandeira, R.M. Moreira, O.R. Mattos, New insights on the role of CO2 in the mechanism of carbon steel corrosion, Corrosion Science 120 (2017) 239–250.